# Pseudospin versus magnetic dipole moment ordering in the isosceles triangular lattice material K$_3$Er(VO$_4$)$_2$

Danielle R. Yahne,[1,*] Liurukara D. Sanjeewa ◉,[2] Athena S. Sefat,[2] Bradley S. Stadelman ◉,[3] Joseph W. Kolis,[3]
Stuart Calder,[4] and Kate A. Ross[1,5,†]

[1]*Department of Physics, Colorado State University, 200 W. Lake St., Fort Collins, Colorado 80523-1875, USA*
[2]*Materials Science and Technology Division, Oak Ridge National Laboratory, Oak Ridge, Tennessee 37831, USA*
[3]*Department of Chemistry, Clemson University, Clemson, South Carolina 29634-0973, USA*
[4]*Neutron Scattering Division, Oak Ridge National Laboratory, Oak Ridge, Tennessee 37831, USA*
[5]*Quantum Materials Program, CIFAR, Toronto, Ontario M5G 1Z8, Canada*

Spin-1/2 antiferromagnetic triangular lattice models are paradigms of geometrical frustration, revealing very different ground states and quantum effects depending on the nature of anisotropies in the model. Due to strong spin orbit coupling and crystal field effects, rare-earth ions can form pseudospin-1/2 magnetic moments with anisotropic single-ion and exchange properties. Thus, rare-earth-based triangular lattices enable the exploration of this interplay between frustration and anisotropy. Here we study one such case, the rare-earth double vanadate glaserite material K$_3$Er(VO$_4$)$_2$, which is a quasi-two-dimensional (2D) isosceles triangular antiferromagnet. Our specific heat and neutron powder diffraction data from K$_3$Er(VO$_4$)$_2$ reveal a transition to long range magnetic order at $T_N = 155 \pm 5$ mK which accounts for all $R \ln 2$ entropy. We observe what appears to be a coexistence of three-dimensional (3D) and quasi-2D order below $T_N$. The quasi-2D order leads to an anisotropic Warren-like peak profile for $(hk0)$ reflections, while the 3D order is best-described by layers of antiferromagnetic $b$-aligned moments alternating with layers of zero moment. Our magnetic susceptibility data reveal that Er$^{3+}$ takes on a strong $XY$ single-ion anisotropy in K$_3$Er(VO$_4$)$_2$, leading to vanishing moments when *pseudospins* are oriented along $c$. Thus, the magnetic structure, when considered from the pseudospin point of view could comprise of alternating layers of $b$-axis and $c$-axis aligned antiferromagnetism.

## I. INTRODUCTION

Magnetic frustration has been of interest in condensed matter physics due to the presence of competing interactions, which often leads to exotic properties. A two-dimensional (2D) triangular lattice with antiferromagnetically (AFM) interacting Ising spins is the simplest example of geometrical frustration. Wannier found in 1950 that this model has a macroscopically degenerate ground state and the frustration suppresses order down to zero temperature [1]. A quantum spin liquid (QSL) state, which exhibits quantum entanglement and fractionalized excitations, was first envisioned by Anderson to exist on a 2D triangular Heisenberg AFM (HAFM) [2]. It is now understood that this model leads to 120° order [3–5], but exchange interaction anisotropies or lattice distortions can lead to other interesting phenomena. For example, the isosceles triangular AFM Cs$_2$CuCl$_4$ was found to be a one-dimensional (1D) spin chain and is an example of "dimensional reduction" induced by frustration [6,7], and anisotropic exchange models on the triangular lattice have been proposed to host QSL phases [8–12].

Rare-earth-based frustrated materials have become of interest due to strong spin orbit coupling and crystal elec-

tric field (CEF) effects which can lead to $S_{\text{eff}} = \frac{1}{2}$ doublets (pseudospin-1/2) and anisotropic effective exchange models based on these pseudospin-1/2 moments. This makes them ideal to study quantum phases arising from anisotropic exchange. The relationship between the observed magnetic dipole moments ($\mu_i$) and the pseudospin-1/2 operators ($S_i$) is given by the $g$-tensor: $\mu_i = g_{ii}S_i$.[1] Depending on the details of the CEF Hamiltonian, the ground-state doublet forming the pseudospins can have certain $g$ components become vanishingly small (or in some cases, identically zero due to the symmetry) and thus no appreciable magnetic dipole moment associated with that pseudospin direction [13]. In the case where the symmetry prevents any dipole moment, these pseudospin directions are associated with higher multipoles, such as quadrupoles [14,15] or octupoles [16–19].

In terms of the search for quantum magnetic phases based on rare-earth ions, Yb$^{3+}$ has received the most attention. For instance, Yb$_2$Ti$_2$O$_7$ was proposed as a quantum spin ice material [20–23], but was later shown to be an unusual ferromagnet with continuumlike scattering [24–26] that appears to arise from phase competition and nonlinear spin wave

---

*danielle.harris@colostate.edu
†kate.ross@colostate.edu

[1]This assumes the $g_{ii}$ values are those obtained from the square root of the eigenvalues of the $G$ tensor [65], so the moment directions defined here by $i$ are along the eigenvectors of that tensor
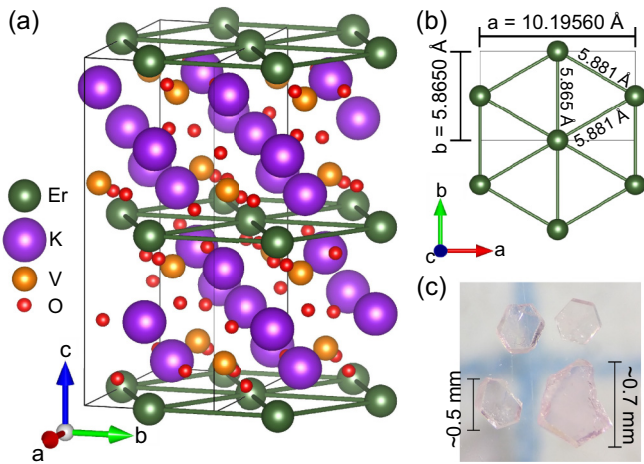
FIG. 1. (a) Crystal structure of monoclinic $K_3Er(VO_4)_2$ (space group $C2/c$) showing layers of 2D isosceles triangular $Er^{3+}$ lattices. (b) The 2D isosceles triangular $Er^{3+}$ lattice, with bond lengths and unit cell size shown (not shown, $c = 15.2050$ Å). (c) Typical single crystals of $K_3Er(VO_4)_2$ which were coaligned for magnetization and susceptibility measurements.

effects [27–29]. Meanwhile, the triangular lattice $YbMgGaO_4$ was proposed as a QSL, but may instead exhibit a random valence bond state due to Mg/Ga site disorder [8,30–35]. Frustrated $Er^{3+}$ materials are also of interest, and the pyrochlores ($Er_2B_2O_7$, $B =$ Ti, Sn, Ge, Pt, etc.) [36–45] have enjoyed the most attention, but other frustrated geometries realized by $Er^{3+}$ are just beginning to be explored [46,47]. Here we study the isosceles triangular material $K_3Er(VO_4)_2$ and show that it has strong $XY$ single-ion anisotropy with an unconventional magnetic ground state described by alternating ordered layers of antiferromagnetic "magnetic dipole active" and "magnetic dipole silent" pseudospins.

$K_3Er(VO_4)_2$ is a member of the rare-earth double vanadate glaserite family, $K_3RE(VO_4)_2$, where $RE = $ (Sc, Y, Dy, Ho, Er, Yb, Lu, or Tm). Previous studies on rare-earth double *phosphate* glaserites [$K_3RE(PO_4)_2$] have shown that there can exist structural transitions between trigonal and lower symmetry structures of these compounds (i.e., monoclinic) [48,49]. While previous reports of $K_3Er(VO_4)_2$ describe it in terms of a trigonal space group ($P\bar{3}m1$) at room temperature [50], we found from powder and single crystal x-ray diffraction, as well as low-temperature neutron diffraction, that a monoclinic structure (space group $C2/c$), shown in Figs. 1(a) and 1(b), is appropriate for our samples at all measured temperatures, similar but not identical to $K_3Er(PO_4)_2$ (which forms in space group $P2_1/m$).

## II. EXPERIMENTAL METHOD AND RESULTS

The crystal growth of monoclinic $K_3Er(VO_4)_2$ phase involved two steps. First, powder synthesis targeting a stoichiometric product of $K_3Er(VO_4)_2$ was performed using $K_2CO_3$, $Er_2O_3$, and $(NH_4)VO_3$. A total of 3 g of components were mixed in a stoichiometric ratio of 3:1:4 and ground well using an Agate motor and pestle. The powder mixture was then pressed into pellets and heated to $750°$ C for 80 hours. After the reaction period, the resulting pellets were crushed,
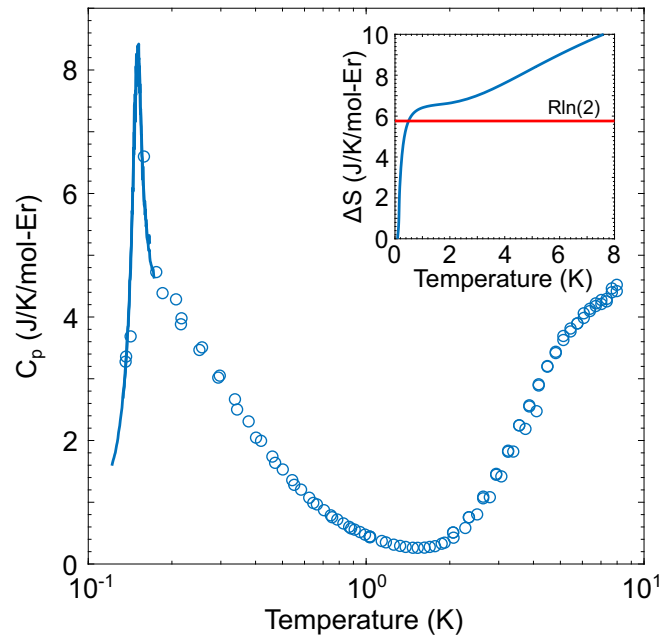


FIG. 2. Single crystal heat capacity in zero magnetic field. The open circles represent the quasiadiabatic measurements, while the solid line represents the long pulse measurements (described in the main text). A sharp magnetic transition is observed at $155 \pm 5$ mK, with the asymmetric shape on the high temperature side of the transition indicating a build-up of low-dimensional short-range correlations. (Inset) Entropy calculated from $C_p$ vs. $T$ with the $R \ln 2$ limit shown, indicating an isolated $S_{\text{eff}} = \frac{1}{2}$ system below 1 K.

ground, and checked the purity using powder x-ray diffraction (PXRD). According to the PXRD, the majority phase was matched with the $K_3Er(VO_4)_2$ (PDF No. 00-51-0095) with impurities of $K_3VO_4$ and $ErVO_4$. In the second step, the resulting $K_3Er(VO_4)_2$ powder was treated hydrothermally to obtain single crystals.

Hydrothermal synthesis was performed using 2.75-inch-long silver tubing that had an inner diameter of 0.375 inches. After the silver tubes were welded shut on one side, the reactants and the mineralizer were added. Next, the silver ampules were welded shut and placed in a Tuttle-seal autoclave that was filled with water to provide appropriate counter pressure. The autoclaves were then heated to $600°$ C for 14 days, reaching an average pressure of 1.7 kbar, utilizing ceramic band heaters. After the reaction period, the heaters were turned off and the autoclave cooled to room temperature. Crystals were recovered by washing with de-ionized water. In a typical reaction 0.4 g of $K_3Er(VO_4)_2$ powder was mixed with a mineralizer solution of 0.8 mL of 10 M $K_2CO_3$.

Crystals of $K_3Er(VO_4)_2$, used for magnetism and heat capacity measurements, were physically examined and selected under an optical microscope equipped with a polarizing attachment. Room-temperature single crystal structures were characterized using a Bruker D8 Venture diffractometer Mo K$\alpha$ radiation ($\lambda = 0.71073$ Å) and a Photon 100 CMOS detector. The Bruker APEX3 software package with SAINT and SADABS routines were used to collect, process, and correct the data for absorption effects. The structures were solved by intrinsic phasing and subsequently refined on $F^2$ using
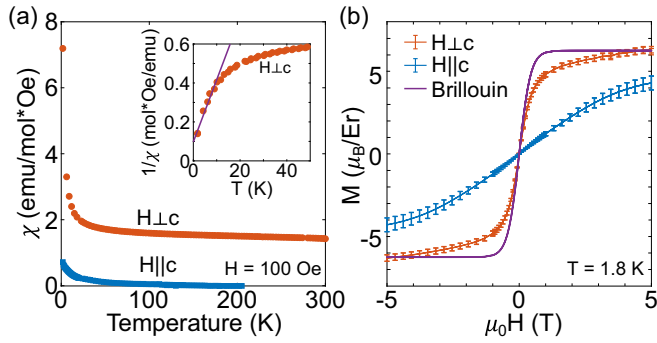
FIG. 3. (a) Magnetic susceptibility of co-aligned single crystals with the field aligned perpendicular and parallel to the $c$-axis, showing $\chi_{\perp c}$ is larger than $\chi_{||c}$ by a factor of $\sim 10$. (Inset) Low-temperature fit of inverse susceptibility used to find the $H \perp c$ Curie-Weiss temperature $\theta_{CW} \approx -3$ K. (b) Magnetization of co-aligned single crystals at 1.8 K. For $H||c$, significant field-induced mixing of the next highest CEF level produces an enhanced moment in the field.

full-matrix least-squares techniques by the SHELXTL software package [51]. All atoms were refined anisotropically (see Appendix A).

We performed heat capacity measurements from 8 K down to 50 mK (Fig. 2) on a $0.41 \pm 0.05$ mg single crystal sample [examples shown in Fig. 1(c)] using a Quantum Design PPMS with dilution refrigerator insert. We employed two measurement techniques, a typical quasiadiabatic thermal relaxation measurement with temperature rise $\Delta T/T$ of 2%, as well as "long pulse" measurements where $\Delta T/T$ can be as large as 400%, as described in Ref. [52]. We find a sharp transition at $T_N = 155 \pm 5$ mK, much lower than the Curie-Weiss temperature (discussed later), indicating that this system is frustrated as expected, with a frustration parameter of $f = \theta_{CW}/T_N \approx 20$. The total $C_p(T)$ (not lattice subtracted) reveals a broad peak around 10 K, the shape of which cannot be purely attributed to a power-law contribution from acoustic phonon modes, as well as a gradual release of entropy on cooling from 1 K down to 155 mK, at which temperature a sharp anomaly is observed. The high-temperature peak near 10 K is indicative of a low-lying excited CEF multiplet with energy of about 2 meV. The entropy change between 50 mK to 2 K accounts for all the entropy expected from a Kramers CEF ground-state doublet ($R \ln 2$ per mole $Er^{3+}$, see inset of Fig. 2). Less than 30% of this entropy is released via the sharp anomaly, indicating that short-range correlations develop over a broad temperature range above the ordering transition. This is commonly found in low-dimensional and frustrated magnets, where ordering is suppressed but is eventually triggered by some subleading energy scale in the Hamiltonian (such as interlayer interactions in the case of quasi-2D systems) [53]. The quasi-2D nature of the magnetism in $K_3Er(VO_4)_2$ is also confirmed by neutron powder diffraction to coexist with 3D order below $T_N$, as discussed later.

The temperature-dependent magnetic susceptibility of $K_3Er(VO_4)_2$ was measured down to 1.8 K in a 100 Oe field [Fig. 3(a)] using the MPMS XL Quantum Design SQUID magnetometer on $1.60 \pm 0.05$ mg and $1.04 \pm 0.10$ mg of co-aligned single crystals, aligned in the $H \perp c$ and $H||c$ di-

rections, respectively. For magnetic fields $H \perp c$, we find net antiferromagnetic interactions shown by the negative Curie-Weiss temperature $\theta_{CW} \approx -3$ K obtained by fitting between 2 and 10 K (although this value is highly dependent on the exact fitting range used due to crystal field effects), similar to YbMgGaO$_4$ with $\theta_{CW} \approx -4$ K. The magnetic susceptibility $\chi_{||c}$ is an order of magnitude less than $\chi_{\perp c}$, indicating a strong $XY$ nature of the $g$-tensor of $Er^{3+}$ in this material. Magnetization measurements [Fig. 3(b)], taken at 1.8 K in a magnetic field up to 5 T, corroborate that $K_3Er(VO_4)_2$ is a strongly $XY$ system due to the large saturation magnetization for $M_{\perp c}$. Neither $M_{\perp c}$ nor $M_{||c}$ follow a Brillouin function expected for a simple paramagnet, suggesting that there is significant mixing of the higher CEF states causing the response to be nonparamagnetic. Due to field-induced mixing of the excited CEF levels, the saturation magnetization is not a good indicator of the zero-field $g$-tensor for either direction. Regardless of the CEF mixing, the magnetization $M_{||c}$ starts with a low $g$-value near zero field, consistent with a small $g$-value in the $c$-axis.

Neutron powder diffraction was performed on the HB-2A beamline at Oak Ridge National Laboratory's (ORNL) High Flux Isotope Reactor (HFIR). Approximately 2.5 g of crystals were ground into a fine powder, placed into a copper sample can, and filled with 10 atm of He gas at room temperature, a technique shown to enable sample thermalization of loose powders below 1 K [54]. Diffraction patterns were obtained from 10 K down to 50 mK, with collimator settings open-open-12', and a Ge(113) monochromator provided an incident wavelength of $\lambda = 2.41$ Å. The patterns were collected over a Q-range of 0.18 Å$^{-1}$ < Q < 4.64 Å$^{-1}$ ($4° < 2\theta < 126°$) with count times of 2 hours per scan.

Analysis of the powder diffraction data was performed using the FULLPROF software suite which implements the Rietveld refinement method [55]. The 10 K data was used to refine the nuclear structure with contributions from the copper cell and aluminum windows masked. Magnetic peaks which could not be indexed within the $K_3Er(VO_4)_2$ unit cell emerged between 10 K and 400 mK, indicating the presence of magnetic impurities in the sample, which were unable to be identified. These impurities are likely to be from by-products produced during the crystal synthesis, which are easy to avoid for single crystals measurements, but is impractical to completely remove for the large sample mass needed for neutron powder measurements. To remove the impurity signal from the magnetic structure analysis, we subtracted the 400 mK data from the 50 mK data, leaving only contributions from $K_3Er(VO_4)_2$ magnetic Bragg peaks [Fig. 5(a)]. The magnetic peaks indexed gave an ordering wavevector of $k = (1, 0, 0)$, for which the decomposition of the magnetic representation into irreducible representations (IR's) is $\Gamma_{mag} = 3\Gamma_1^{(1)} + 0\Gamma_2^{(1)} + 3\Gamma_3^{(1)} + 0\Gamma_4^{(1)}$ for a magnetic atom at site (0.5,0,0.5) found using the SARA$h$ Representational Analysis software [56] (Kovalev tables). $\Gamma_1$ is composed of basis vectors $\psi_{1,2,3}$, and $\Gamma_3$ is composed of basis vectors $\psi_{4,5,6}$. Basis vectors $\psi_{2,4,6}$ have antiferromagnetic (AFM) spin arrangements in the $ab$ plane which are ferromagnetically (FM) correlated along the $c$-axis (i.e., every layer is identical), with moments pointing along the $b$, $a$, and $c$ axes, respectively. $\psi_{1,3,5}$ are AFM in the $ab$ plane as well as along the $c$-axis, with

TABLE I. Irreducible representation and basis vector composition for space group $C2/c$ with $k = (1, 0, 0)$ found using the SARA*h* Representational Analysis software. The atoms are defined according to $m_1$: (0.5,0,0.5) and $m_2$:(0.5,0,0).

| IR | BV | Basis Vector Components | | | | | |
|----|----|-----|-----|-----|-----|-----|-----|
|    |    | $m_{1a}$ | $m_{1b}$ | $m_{1c}$ | $m_{2a}$ | $m_{2b}$ | $m_{2c}$ |
| $\Gamma_1$ | $\psi_1$ | 2 | 0 | 0 | $-2$ | 0 | 0 |
|            | $\psi_2$ | 0 | 2 | 0 | 0 | 2 | 0 |
|            | $\psi_3$ | 0 | 0 | 2 | 0 | 0 | $-2$ |
| $\Gamma_3$ | $\psi_4$ | 2 | 0 | 0 | 2 | 0 | 0 |
|            | $\psi_5$ | 0 | 2 | 0 | 0 | $-2$ | 0 |
|            | $\psi_6$ | 0 | 0 | 2 | 0 | 0 | 2 |

moments pointing along the $a$, $c$, and $b$ axes, respectively. The summary of these basis vectors and their components for each site is in Table I and shown in Fig. 4.

We attempted to fit the magnetic scattering within a single IR, which would be expected for a second-order phase transition [57], however, no linear combination of the basis vectors restricted to a single IR came close to reproducing the observed magnetic structure (Appendix D). It should also be noted that all fits lacked perfect agreement with the intensity of all of the magnetic peaks simultaneously, specifically with respect to the (100) reflection. The shape of the (100) peak does not follow the typical pseudo-Voigt peak shape, and is instead reminiscent of the Warren line-shape for random 2D layered lattices [58], having an asymmetric base that extends further to high $Q$. In a 2D random layer lattice, where no correlations exist between layers, the structure factor for $(hkl)$ zone centers is expected to be zero [58], in contrast to the
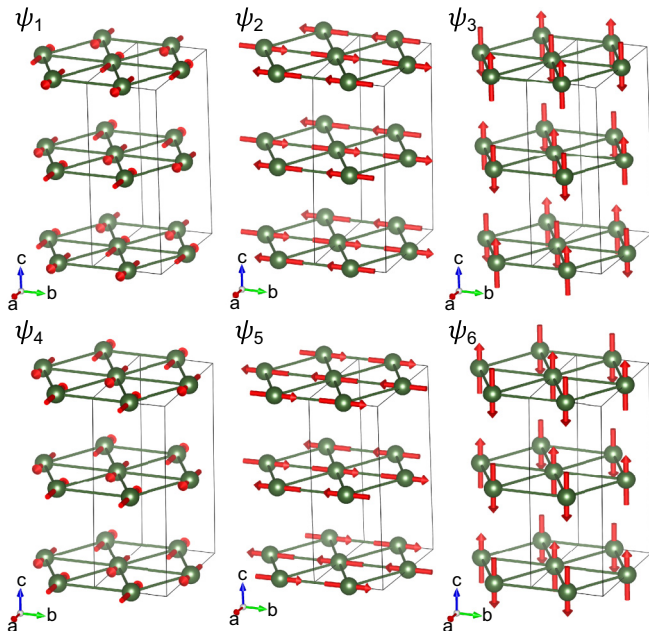


FIG. 4. Visualizations of the basis vectors for space group $C2/c$ with $k = (1, 0, 0)$: $\psi_{1,2,3}$ from $\Gamma_1$ and $\psi_{4,5,6}$ from $\Gamma_3$. All basis vectors are antiferromagnetic in the $ab$-plane. Basis vectors $\psi_{1,3,5}$ are also antiferromagnetic along $c$, while basis vectors $\psi_{2,4,6}$ are ferromagnetic along $c$ (each layer is identical).

$(hk0)$ zone centers, which are nonzero and will have this asymmetric shape. For *quasirandom* 2D layers with some short-range correlations between planes, intensity is expected at $(hkl)$ reflections, but peaks will have suppressed intensities and will, in principle, be broadened compared to a peak arising from long range 3D order [59–61].

As a pure Warren line-shape did not accurately reproduce the (100) reflection, we explored the 2D nature of this material by performing a numerical simulation for the (100) reflection to determine the in-plane and out-of-plane correlation lengths (see Appendix C for details). The simulation of the (100) peak produces an out-of-plane correlation length that is inconsistent with the $(hkl)$ magnetic Bragg peaks, which are almost resolution-limited, indicating there is instead a coexistence of 2D and 3D order in $K_3Er(VO_4)_2$. The origin of this coexistence is unknown, but similar effects have been observed in other materials, where it has been speculated to arise from structural inhomogeneities [62,63]. However, as shown in Fig. 5(b), the 2D and 3D peaks have similar temperature dependence, which indicates that even if there are inhomogeneous regions of 3D and quasi-2D order, they onset at the same temperature.

Due to the contributions from 2D and 3D correlations to the (100) peak, it was excluded from the fit of the 3D magnetic structure. Our refined magnetic structure is given by equal contributions from basis vectors $\psi_2$ (from $\Gamma_1$) and $\psi_5$ (from $\Gamma_3$), with basis vector coefficients 0.90(2). This leads to moments along $b$ that add together in one layer and cancel in the other layer due to the FM and AFM spin correlations along the $c$-axis [Fig. 5(c)]. It should be noted that less prominent contributions of basis vector $\psi_6$, which adds small $c$-aligned moment to the layers, could be included without affecting the fit drastically. From the susceptibility data though, little to no moment is expected out-of-plane, so the $\psi_6$ contribution is expected to be small or zero. Comparing the calculated diffraction pattern to the data [Fig. 5(a)], it is clear that the $(hk0)$ peaks are underestimated. This is as expected since the $(hk0)$ peaks contain significant contributions from the 2D correlations in the material that are not captured by the model.

### III. DISCUSSION

The refined magnetic structure, in conjunction with the heat capacity, which produces the full $R \ln 2$ entropy change upon integrating $C_p/T$ from 50 mK to 1 K, suggests that $K_3Er(VO_4)_2$ is in a fully ordered state, yet the refined structure implies the absence of ordered moments in every other layer. Quantum fluctuations could, in principle, produce reduced or zero moment on some layers, however, a simpler explanation seems to be possible by considering the inferred $g$-tensor and the likely pseudospin order. We suggest that the likely *pseudospin* ordering structure involves the 2D triangular layers alternating between AFM ordered layers with moment along $\vec{b}$ and $\vec{c}$ [Fig. 5(d)].[2] Such a spin structure is not likely to be obtained from purely $XY$ exchange interactions. Yet, because of the strong $XY$ *single-ion* nature of this material ($g_z \sim 0$), the

_____

[2]this *pseudospin* state can be visualized using a combination of $\Psi_{2,5,6}$ and $-\Psi_3$ (Fig. 4).
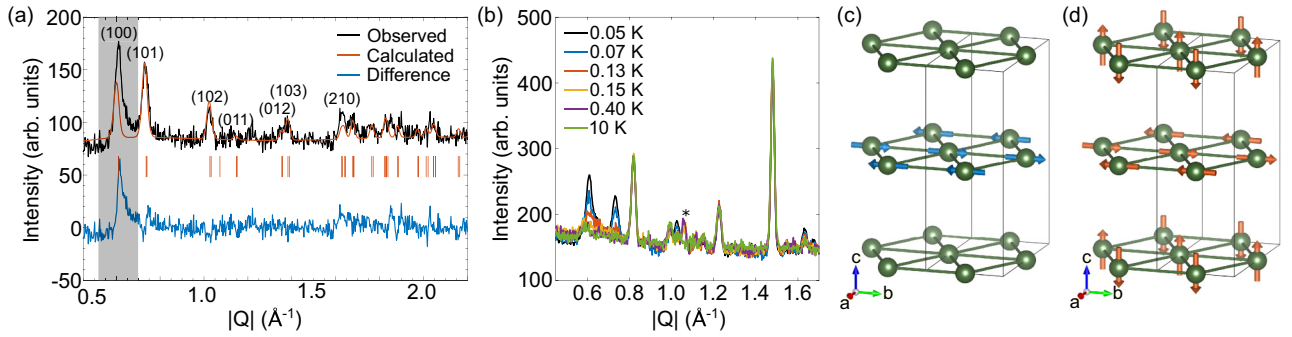
FIG. 5. (a) Neutron diffraction pattern (black) taken on a 2.5-g powder sample on beamline HB-2A at HFIR (ORNL). Magnetic peaks were found from subtracting the 400-mK pattern from the 50-mK pattern to remove impurity signals. A coexistence of 2D and 3D order was found, and thus the Warren-like (100) peak was not included in the fit. The fit to the 3D order (red) and calculated difference (blue) is shown for the best fit using the FULLPROF software, which was a linear combination of equal contributions of basis vectors $\psi_2$ (from $\Gamma_1$) and $\psi_5$ (from $\Gamma_3$). (b) Temperature dependence of magnetic Bragg peaks below the transition temperature of 155 mK shows the onset of 2D and 3D order occurs at the same temperature. Magnetic impurity peaks were found between 10 and 400 mK, denoted with a star. (c) The magnetic structure found from neutron diffraction pattern shows layers of $b$-aligned moment alternating with layers of zero moment, proposed to be due to the strong $XY$ nature of $K_3Er(VO_4)_2$ ($g_z \sim 0$). (d) The proposed *pseudospin* structure, alternating between layers of $b$-aligned pseudospin and layers of $c$-aligned pseudospin.

layers with the pseudospins pointing along the $c$-axis would carry approximately zero dipole moment and thus appear to be disordered (or strongly reduced) according to probes that are sensitive only to dipole magnetic moments, such as neutron scattering. This result emphasizes a subtle point which is sometimes misunderstood; the $g$-tensor anisotropy of pseudospin-1/2 systems does not need to be the same as the exchange anisotropy.

Similar effects are at play in some rare-earth pyrochlores, where the the $XY$ part of the pseudospin carries a quadrupolar [14,15] or octupolar [16–19] moment but no dipole moment. However, even "conventional" Kramer's doublets which transform as dipoles in all directions can have very small $g$-values in certain directions [13], which is the case for $Er^{3+}$ in $Er_2Sn_2O_7$ [38]. Due to the low point symmetry at the $Er^{3+}$ site (triclinic) of $K_3Er(VO_4)_2$, the ground-state CEF doublet is most likely to be a conventional Kramer's doublet. This could, in principle, be investigated by an analysis of the CEF levels in the material, however, we note that the point symmetry for $Er^{3+}$ in $K_3Er(VO_4)_2$ is triclinic, leading to 15 symmetry-allowed Steven's parameters which will likely require the combination of multiple types of measurements (for instance EPR and inelastic neutron scattering) to uniquely determine.

## IV. CONCLUSION

We performed an extensive study of the magnetic properties of a member of the rare-earth double vanadate glaserite materials, which form 2D isosceles (or equilateral, in the case of the trigonal polymorphs) triangular lattices. We found an antiferromagnetic transition in $K_3Er(VO_4)_2$ at 155 mK despite a relatively strong AFM interaction of 3 K inferred from Curie-Weiss analysis (frustration parameter $f \sim 20$). Susceptibility measurements reveal this material to have strong $XY$ $g$-tensor anisotropy, although field-induced coupling to a low-lying CEF level near $\sim$2 meV [inferred from $C_p(T)$] hinders a quantitative estimate of the $g$-tensor via magnetization. The magnetic structure is likely comprised of large AFM magnetic

dipole moments ordering along the $b$-axis direction in every other layer, and magnetic dipole suppressed pseudospin order along $c$ in the other layers. In this light, $K_3Er(VO_4)_2$ thus appears to be one of the clearest examples in which pseudospin order results in zero dipole moments. Inelastic neutron scattering studies of $K_3Er(VO_4)_2$ could help to validate this model, and could also reveal the inferred low lying CEF level. Furthermore, the measurement of the $g$-tensor via electron paramagnetic resonance could help to confirm our proposed model. Further studies of other rare-earth glaserites, particularly in their trigonal structural polymorphs, would be intriguing, as they could be promising materials for discovering new quantum magnetic phases due to their pseudospin-1/2 angular momentum and strong frustration.

## APPENDIX A: SAMPLE PREPARATION

Crystallographic data for monoclinic $K_3Er(VO_4)_2$ was determined using single crystal x-ray diffraction, the details of which are outlined in the main text, and the results are shown in Table II. A large number of single crystals of $K_3Er(VO_4)_2$ were ground into a powder for neutron diffraction using a mortar and pestle. Due to the large number of crystals necessary to achieve a substantial mass for neutron scattering,

TABLE II. Crystallographic data of $K_3Er(VO_4)_2$ determined by single crystal x-ray diffraction.

| Empirical formula | $K_3Er(VO_4)_2$ |
|---|---|
| Formula weight (g/mol) | 514.44 |
| Crystal system | Monoclinic |
| Crystal dimensions, mm | 0.10 x 0.02 x 0.02 |
| Space group, Z | $C2/c$ (no.15), 4 |
| T, K | 298 |
| a, Å | 10.1956(4) |
| b, Å | 5.8650(2) |
| c, Å | 15.2050(6) |
| $\beta$,° | 90.12(1) |
| Volume, Å³ | 909.21(6) |
| $D$(calc), g/cm³ | 3.758 |
| $\mu$ (Mo K$\alpha$), mm⁻¹ | 12.543 |
| $F(000)$ | 940 |
| $T_{max}, T_{min}$ | 1.0000, 0.8169 |
| $2\theta$ range | 2.679–24.990 |
| Reflections collected | 10581 |
| Data/restraints/parameters | 781/0/67 |
| Final R $[I > 2\sigma(I)]$ $R_1$, $R_{w2}$ | 0.0372, 0.1144 |
| Final R (all data) $R_1$, $R_{w2}$ | 0.0374, 0.1144 |
| GoF | 1.086 |
| Largest diff. peak/hole, e/ Å³ | 1.760/−1.155 |

the crystals were ground in three batches, which were x-rayed separately and then again after the batches were combined. Powder x-ray diffraction was performed on a Bruker D8 Discover Davinci diffractometer from $10° < 2\theta < 60°$ for approximately 1 s per 0.02°. The PXRD pattern was fit using TOPAS Rietveld refinement, and was found to be in agreement with the single crystal XRD. No preferred orientation or peak broadening were found, indicating the crystals were ground sufficiently. Impurity peaks were unable to be matched with any of the expected by-products ($ErVO_4$, $Er_3O_2$, etc.), and are likely to be from by-products introduced during the hydrothermal synthesis. The powder was then shipped to ORNL where it was placed into a copper sample can. The sample can was fitted with a piece of indium within the He filling line to allow the can to be filled with 10 atm of He gas and then crimped at the indium, thereby containing the gas.

## APPENDIX B: LOW-TEMPERATURE NUCLEAR STRUCTURE

Neutron powder diffraction was performed at 10 K and was used to determine the low-temperature lattice parameters. The neutron data corroborates that the monoclinic space group best describes the crystal structure (Fig. 6). As expected, we find small impurity peaks in the nuclear data, denoted by stars, and do not find any evidence of preferred orientation. Upon decreasing the temperature to 400 mK, *magnetic* impurity peaks were found, specifically evidenced by a peak at $|Q| = 1.06$ Å that increases in intensity between 10 K and 400 mK, and does not increase intensity further upon cooling to 50 mK [Fig. 5(b)]. Due to the different onset temperature and no signatures of a transition between 10 K and 400 mK in the heat capacity data, this is not believed to be a secondary
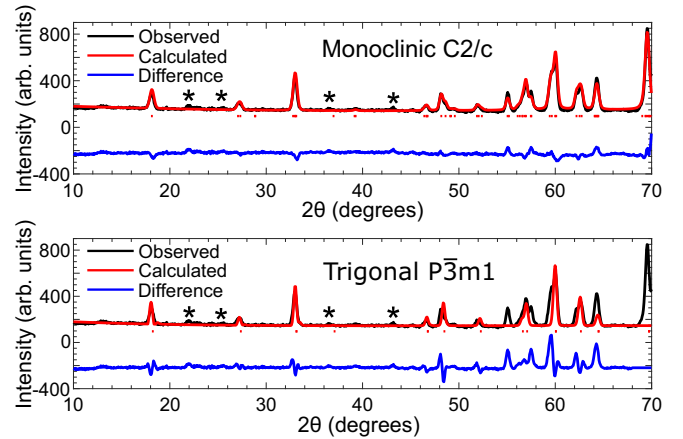


FIG. 6. Nuclear structure refinement of $K_3Er(VO_4)_2$ neutron diffraction data taken at 10 K. The trigonal structure clearly does not describe the crystal structure in contrast to the monoclinic structure. The impurity is also seen in small peaks unable to be fit by either structure, denoted by stars.

phase of $K_3Er(VO_4)_2$. To remove this unknown impurity, we subtracted the 400 mK data from the 50 mK data, leaving only the magnetic scattering signal to be analyzed.

## APPENDIX C: QUASI-2D SIMULATION

The first magnetic peak, (100), does not have the expected pseudo-Voigt peak shape and instead follows more of Warren line-shape for random 2D layer lattices. The Warren line-shape comes from rods of scattering in reciprocal space, centered at $(hk)$. Initially, we attempted to fit the (100) peak with a Warren function [58,64], but the Warren fit overestimated the high $Q$ tail [Fig. 7(a)]. In addition, a lattice with perfectly random 2D layers (i.e. no correlations along the $c$-axis) will have only non-zero structure factors for $(hk0)$ peaks,
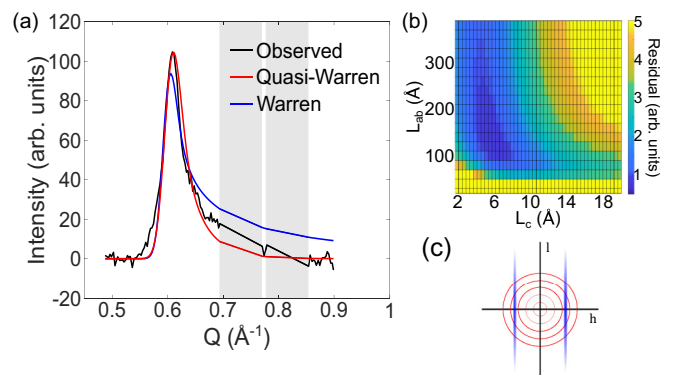


FIG. 7. (a) Warren fit and quasi-Warren simulation of the (100) peak from the 50-mK neutron diffraction data (not background subtracted). The neighboring $(hkl)$ and nuclear peaks were masked (grey boxes). The Warren fit overestimates the high-$Q$ side of the asymmetric $(hk0)$ peak, while the quasi-Warren simulation fails to capture the $(hkl)$ peak shape (discussed in text). (b) Residual plot for combinations of correlation lengths along the $ab$ and $c$ directions. (c) 2D visualization of simulation in the $h0l$ plane, where blue ellipses are the scattering intensities and the red circles are the integrated areas simulating the powder diffraction.

while $(hkl)$ peaks would have zero intensity. As our magnetic diffraction data includes $(hkl)$ peak intensity, this suggests that the layers could have some short-range correlations along $c$, and the layers are instead *quasi*-random. Quasirandom 2D layers would still posses asymmetrical $(hk0)$ peaks, while $(hkl)$ peaks would be suppressed and broadened, but nonzero. We used a numerical simulation, which we call the quasi-Warren simulation, to estimate the in-plane and out-of-plane correlations and fit the (100) asymmetric peak, which shows that this is *not* the case, as discussed next. Thus we infer that the magnetic correlations are a possibly inhomogeneous mixture of 2D and 3D orders.

The numerical simulation was performed by creating a 3D Gaussian ellipse (instead of rods) at zone centers in reciprocal space using the unit cell parameters found from the neutron diffraction taken at 10 K [Fig. 7(c)]. The variables of this ellipse were the standard deviations in the $ab$ and $c$ directions which are related to the correlations in the $ab$ plane, $L_{ab}$, and the correlations between planes, $L_c$, respectively by the equation $L = \sqrt{2\ln 2}/\sigma$. A radial integral was performed to simulate the powder-averaged neutron diffraction pattern, the result of which was then scaled by a Lorentz factor (geometrical correction) and the magnetic form factor. This was then convolved with the instrument resolution, estimated by the FWHM of a nearby nuclear peak. The peak height was scaled to the data, and the results compared to the Warren fit are shown in Fig. 7(a).

The simulation finds a range of correlation lengths fit the data well [Fig. 7(b)], but a best fit estimates correlation lengths along the $c$ axis $L_c \approx 6$ Å (approximately half a unit cell), while correlations in the $ab$ plane $L_{ab} \approx 120$ Å (more than 20 unit cells). When these correlation lengths are applied to an $(hkl)$ peak, we find the peak would be much broader and significantly more suppressed than what we observe. Thus, the 2D and 3D orders must be coexisting and onset at the same temperature.

### APPENDIX D: MAGNETIC STRUCTURE

We attempted to fit the magnetic structure using a single IR, as it was not clear if the transition found in heat capacity was a first- or second-order transition. Examples of those fits are shown in Fig. 8. Both fits of individual IR's had peaks which were not seen in the scattering signal, while the accepted fit (combination of $\psi_2$ from $\Gamma_1$ and $\psi_5$ from $\Gamma_3$) does not show any spurious peaks. In the scenario where the magnetic structure is a combination of more than one IR, it follows that the transition must be first-order.

The fit may also be described in terms of magnetic space groups. Using this approach gives two magnetic space groups that are maximally allowed, $Pc2_1/c$ and $Pc2/c$. As these only have one Er site, it is not possible to recreate the magnetic structure only using one magnetic space group, similarly to what we find using the irreducible representation analysis. However, a subgroup of lower symmetry could be used, namely the magnetic space group $Ps1$ which has two inequivalent Er sites and would be able to recreate the found magnetic structure. This would imply some sort of subtle structural distortion beyond the limits of the measurements performed. This is consistent with our observation that two IR's must be
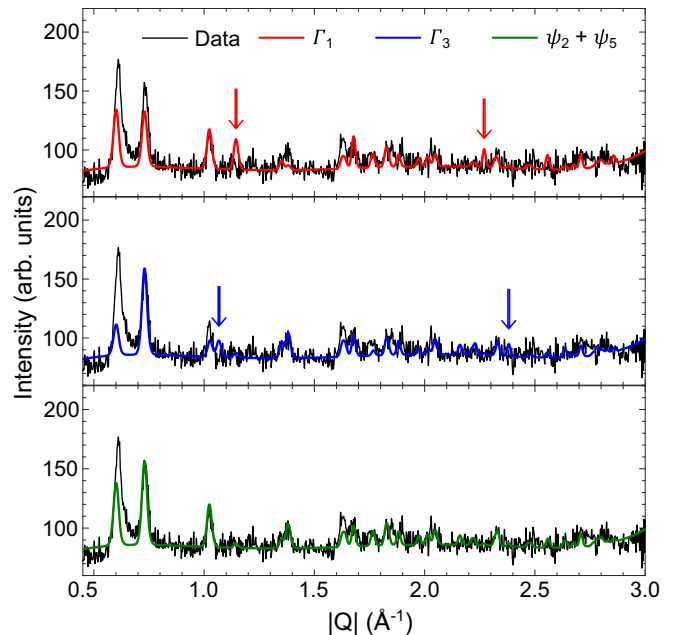


FIG. 8. Examples of fits using a single irreducible representation. Both $\Gamma_1$ and $\Gamma_3$ fits give peaks not seen in the data, shown by arrows. Therefore, the best fit comes from a linear combination of $\Gamma_1$ and $\Gamma_3$'s basis vectors, $\psi_2$ and $\psi_5$ respectively.

mixed to account for the observed Bragg intensity. Such a mixed-IR magnetic structure can only arise if the symmetry is lower than assumed, which could happen at a first-order transition.

The data were fit at multiple temperatures and the total moment was able to be extracted as a function of temperature, shown in Fig. 9 to be approximately $4\mu_B$. Due to the low point density of the total moment as a function of temperature, it is difficult to fit the order parameter equation, but we included a guide to the eye. The total moment is lower than the saturated moment of $6.2\mu_B$ found from magnetization, but we know the saturated moment will be increased by the field-induced mixing of the low-lying crystal field level.
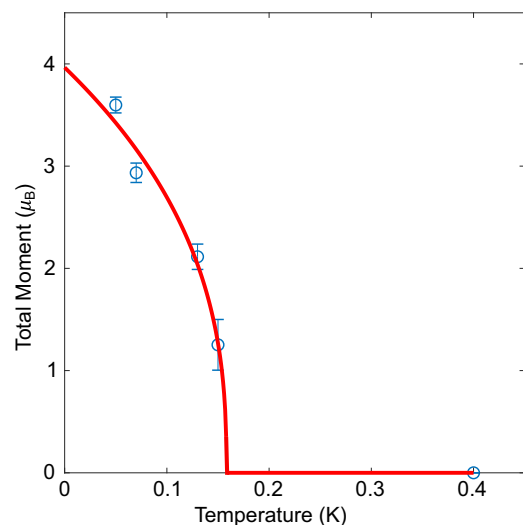


FIG. 9. Total moment as a function of temperature. Red line serves as an order parameter guide to the eye (note this is not a fit).

[1] G. H. Wannier, Phys. Rev. **79**, 357 (1950).

[2] P. W. Anderson, Mater. Res. Bull. **8**, 153 (1973).

[3] B. Bernu, C. Lhuillier, and L. Pierre, Phys. Rev. Lett. **69**, 2590 (1992).

[4] L. Capriotti, A. E. Trumper, and S. Sorella, Phys. Rev. Lett. **82**, 3899 (1999).

[5] S. R. White and A. L. Chernyshev, Phys. Rev. Lett. **99**, 127004 (2007).

[6] R. Coldea, D. A. Tennant, A. M. Tsvelik, and Z. Tylczynski, Phys. Rev. Lett. **86**, 1335 (2001).

[7] L. Balents, Nature **464**, 199 (2010).

[8] Z. Zhu, P. A. Maksimov, S. R. White, and A. L. Chernyshev, Phys. Rev. Lett. **119**, 157201 (2017).

[9] J. Iaconis, C. Liu, G. B. Halász, and L. Balents, SciPost Phys. **4**, 003 (2018).

[10] Z. Zhu, P. A. Maksimov, S. R. White, and A. L. Chernyshev, Phys. Rev. Lett. **120**, 207203 (2018).

[11] M. Bordelon, E. Kenney, T. Hogan, L. Posthuma, M. Kavand, Y. Lyu, M. Sherwin, C. Brown, M. J. Graf, L. Balents, and S. D. Wilson, Nat. Phys. **15**, 1058 (2019).

[12] R. Zhong, S. Guo, G. Xu, Z. Xu, and R. J. Cava, PNAS **116**, 14505 (2019).

[13] J. G. Rau and M. J. P. Gingras, Ann. Rev. Condens. Matter Phys. **10**, 357 (2019).

[14] S. Onoda and Y. Tanaka, Phys. Rev. B **83**, 094411 (2011).

[15] S. Petit, E. Lhotel, S. Guitteny, O. Florea, J. Robert, P. Bonville, I. Mirebeau, J. Ollivier, H. Mutka, E. Ressouche, C. Decorse, M. Ciomaga Hatnean, and G. Balakrishnan, Phys. Rev. B **94**, 165153 (2016).

[16] Y.-P. Huang, G. Chen, and M. Hermele, Phys. Rev. Lett. **112**, 167203 (2014).

[17] E. Lhotel, S. Petit, S. Guitteny, O. Florea, M. Ciomaga Hatnean, C. Colin, E. Ressouche, M. R. Lees, and G. Balakrishnan, Phys. Rev. Lett. **115**, 197202 (2015).

[18] Y.-d. Li, X. Wang, and G. Chen, Phys. Rev. B **94**, 201114(R) (2016).

[19] Y.-D. Li and G. Chen, Phys. Rev. B **95**, 041106(R) (2017).

[20] K. A. Ross, L. Savary, B. D. Gaulin, and L. Balents, Phys. Rev. X **1**, 021002 (2011).

[21] R. Applegate, N. R. Hayre, R. R. P. Singh, T. Lin, A. G. R. Day, and M. J. P. Gingras, Phys. Rev. Lett. **109**, 097205 (2012).

[22] N. R. Hayre, K. A. Ross, R. Applegate, T. Lin, R. R. P. Singh, B. D. Gaulin, and M. J. P. Gingras, Phys. Rev. B **87**, 184423 (2013).

[23] A. Scheie, J. Kindervater, S. Säubert, C. Duvinage, C. Pfleiderer, H. J. Changlani, S. Zhang, L. Harriger, K. Arpino, S. M. Koohpayeh, O. Tchernyshyov, and C. Broholm, Phys. Rev. Lett. **119**, 127201 (2017).

[24] L. J. Chang, S. Onoda, Y. Su, Y. J. Kao, K. D. Tsuei, Y. Yasui, K. Kakurai, and M. R. Lees, Nat. Commun. **3**, 992 (2012).

[25] E. Lhotel, S. R. Giblin, M. R. Lees, G. Balakrishnan, L. J. Chang, and Y. Yasui, Phys. Rev. B **89**, 224419 (2014).

[26] J. Gaudet, K. A. Ross, E. Kermarrec, N. P. Butch, G. Ehlers, H. A. Dabkowska, and B. D. Gaulin, Phys. Rev. B **93**, 064406 (2016).

[27] J. Robert, E. Lhotel, G. Remenyi, S. Sahling, I. Mirebeau, C. Decorse, B. Canals, and S. Petit, Phys. Rev. B **92**, 064425 (2015).

[28] J. D. Thompson, P. A. McClarty, D. Prabhakaran, I. Cabrera, T. Guidi, and R. Coldea, Phys. Rev. Lett. **119**, 057203 (2017).

[29] J. G. Rau, R. Moessner, and P. A. McClarty, Phys. Rev. B **100**, 104423 (2019).

[30] Y. Li, H. Liao, Z. Zhang, S. Li, F. Jin, L. Ling, L. Zhang, Y. Zou, L. Pi, Z. Yang *et al.*, Sci. Rep. **5**, 16419 (2015).

[31] Y. Shen, Y. D. Li, H. Wo, Y. Li, S. Shen, B. Pan, Q. Wang, H. C. Walker, P. Steffens, M. Boehm, Y. Hao, D. L. Quintero-Castro, L. W. Harriger, M. D. Frontzek, L. Hao, S. Meng, Q. Zhang, G. Chen, and J. Zhao, Nature **540**, 559 (2016).

[32] J. A. Paddison, M. Daum, Z. Dun, G. Ehlers, Y. Liu, M. B. Stone, H. Zhou, and M. Mourigal, Nat. Phys. **13**, 117 (2017).

[33] Y.-D. Li, Y.-M. Lu, and G. Chen, Phys. Rev. B **96**, 054445 (2017).

[34] I. Kimchi, A. Nahum, and T. Senthil, Phys. Rev. X **8**, 031028 (2018).

[35] W. M. Steinhardt, Z. Shi, A. Samarakoon, S. Dissanayake, D. Graf, Y. Liu, W. Zhu, C. Marjerrison, C. D. Batista, and S. Haravifard, arXiv:1902.07825

[36] M. E. Zhitomirsky, M. V. Gvozdikova, P. C. W. Holdsworth, and R. Moessner, Phys. Rev. Lett. **109**, 077204 (2012).

[37] L. Savary, K. A. Ross, B. D. Gaulin, J. P. C. Ruff, and L. Balents, Phys. Rev. Lett. **109**, 167201 (2012).

[38] S. Guitteny, S. Petit, E. Lhotel, J. Robert, P. Bonville, A. Forget, and I. Mirebeau, Phys. Rev. B **88**, 134408 (2013).

[39] K. A. Ross, Y. Qiu, J. R. D. Copley, H. A. Dabkowska, and B. D. Gaulin, Phys. Rev. Lett. **112**, 057201 (2014).

[40] X. Li, W. M. Li, K. Matsubayashi, Y. Sato, C. Q. Jin, Y. Uwatoko, T. Kawae, A. M. Hallas, C. R. Wiebe, A. M. Arevalo-Lopez, J. P. Attfield, J. S. Gardner, R. S. Freitas, H. D. Zhou, and J.-G. Cheng, Phys. Rev. B **89**, 064409 (2014).

[41] Z. L. Dun, X. Li, R. S. Freitas, E. Arrighi, C. R. Dela Cruz, M. Lee, E. S. Choi, H. B. Cao, H. J. Silverstein, C. R. Wiebe, J. G. Cheng, and H. D. Zhou, Phys. Rev. B **92**, 140407(R) (2015).

[42] Y. Q. Cai, Q. Cui, X. Li, Z. L. Dun, J. Ma, C. delaCruz, Y. Y. Jiao, J. Liao, P. J. Sun, Y. Q. Li, J. S. Zhou, J. B. Goodenough, H. D. Zhou, and J. G. Cheng, Phys. Rev. B **93**, 014443 (2016).

[43] J. G. Rau, S. Petit, and M. J. P. Gingras, Phys. Rev. B **93**, 184408 (2016).

[44] S. Petit, E. Lhotel, F. Damay, P. Boutrouille, A. Forget, and D. Colson, Phys. Rev. Lett. **119**, 187202 (2017).

[45] A. M. Hallas, J. Gaudet, N. P. Butch, G. Xu, M. Tachibana, C. R. Wiebe, G. M. Luke, and B. D. Gaulin, Phys. Rev. Lett. **119**, 187201 (2017).

[46] Y. Cai, C. Lygouras, G. Thomas, M. N. Wilson, J. Beare, D. R. Yahne, K. Ross, Z. Gong, Y. J. Uemura, H. A. Dabkowska, and G. M. Luke, Phys. Rev. B **101**, 094432 (2020).

[47] Y. Cai, M. N. Wilson, J. Beare, C. Lygouras, G. Thomas, D. R. Yahne, K. Ross, K. M. Taddei, G. Sala, H. A. Dabkowska, A. A. Aczel, and G. M. Luke, Phys. Rev. B **100**, 184415 (2019).

[48] S. V. Ushakov, A. Navrotsky, J. M. Farmer, and L. A. Boatner, J. Mater. Res. **19**, 2165 (2004).

[49] I. Szczygieł, A. Matraszek, and T. Znamierowska, J. Therm. Anal. Cal. **93**, 671 (2008).

[50] M. M. Kimani, L. Thompson, W. Snider, C. D. McMillen, and J. W. Kolis, Inorg. Chem. **51**, 13271 (2012).

[51] G. M. Sheldrick, Acta Cryst. **A71**, 3 (2015).

[52] A. Scheie, J. Low Temp. Phys. **193**, 60 (2018).

[53] L. J. de Jongh (ed.), *Magnetic Properties of Layered Transition Metal Compounds*, Vol. 9 (Springer, Amsterdam, 1990).

[54] D. H. Ryan and I. P. Swainson, J. Appl. Cryst. **42**, 43 (2009).

[55] J. Rodríguez-Carvajal, Physica B **192**, 55 (1993).

[56] A. S. Wills, Physica B **276-278**, 680 (2000).

[57] A. Wills, J. Phys. IV (France) **11**, Pr9-133 (2001).

[58] B. E. Warren, Phys. Rev. **59**, 693 (1941).

[59] J. Pappis and S. L. Blum, J. Am. Ceram. Soc. **44**, 592 (1961).

[60] H. Shi, J. N. Reimers, and J. R. Dahn, J. Appl. Crystallogr. **26**, 827 (1993).

[61] H. Fujimoto, Carbon **41**, 1585 (2003).

[62] V. O. Garlea, A. T. Savici, and R. Jin, Phys. Rev. B **83**, 172407 (2011).

[63] V. O. Garlea, M. A. McGuire, L. D. Sanjeewa, D. M. Pajerowski, F. Ye, and J. W. Kolis, AIP Adv. **8**, 101407 (2018).

[64] A. S. Wills, A. Harrison C. Ritter, and R. I. Smith, Phys. Rev. B **61**, 6156 (2000).

[65] A. Abragam and B. Bleaney, *Electron Paramagnetic Resonance of Transition Ions* (Oxford University Press, New York, 1970).

*Correction:* The omission of a support statement in the Acknowledgments section has been fixed.